Quantifying Stern Layer Water Alignment Prior to and During the Oxygen Evolution Reaction

Raiden Speelman and Franz M. Geiger*

Department of Chemistry, Northwestern University,

2145 Sheridan Road, Evanston, IL 60660, USA

Abstract. While water's oxygen is the electron source in the industrially important oxygen evolution reaction, the strong absorber problem clouds our view of how the Stern layer water molecules orient themselves in response to applied potentials. Here, we report nonlinear optical measurements on nickel electrodes held at pH 13 indicating a disorder-to-order transition in the Stern layer water molecules prior to the onset of Faradaic current. A full water monolater (1.1 x 10^{15} cm^{-2}) aligns with oxygen atoms pointing towards the electrode at +0.8 V and the associated work is 80 kJ mol^{-1}. Our experiments identify water flipping energetics as a target for understanding overpotentials, advance molecular electrochemistry, provide benchmarks for electrical double layer models, and serve as a diagnostic tool for understanding electrocatalysis.

Main. Much microscopic insight into the Stern layer water structure and the electric fields at electrolyte:electrode interfaces currently comes from atomistic simulations (*1-7*), with joint theoretical and surface-specific experimental studies just emerging (*8-12*). Probing interfacial solvent structure and electrostatic fields at electrode:electrolyte interfaces directly, in real time, and without the need for electrochemical, spin, or spectroscopic labels, plasmonic structures, or arbitrarily chosen reference states remains a major challenge despite the topic's importance for many electrochemical transformations (*7, 13-18*). The major challenge is water's strong absorber problem, complicating the detection of water's stretching and bending modes at electrode:electrolyte interfaces. Compounding the problem is that linear spectroscopies are

insensitive to whether water molecules point one way or the other. Non-resonant second-order optical techniques could overcome these issues and be the method of choice for probing water orientation and flipping in response to applied potentials.

Consider the amphoteric nature of the oxides that terminate many electrodes used for the oxygen evolution reaction. This reaction is typically carried out at high pH (*19*) where, at open circuit potential, many of the interfacial water molecules point their protons to the electrode surface. In this configuration, access of the electrode's active sites to the electrons in water's oxygen atoms would be blocked by water's protons. An externally applied potential would need to be sufficiently high to weaken the interfacial hydrogen bond network so that the water molecules can flip to point their electron source (the oxygen atoms) towards the electrode's active site (the high oxidation state metal oxo site). The energy associated with water flipping is a likely contributor to the water oxidation overpotential.

The sensitivity of nonlinear optical processes to interfacial structure and electrostatics should make it possible to quantify and track the number of Stern layer water molecules that are flipping, and the associated energetics, as a function of the applied potential, provided the strong absorber problem can be overcome. Given the prominent role of water's oxygen atoms as an earth-abundant electron source and the aforementioned need for water flipping to access them, quantifying how 1) the number net of-aligned water molecules, 2) the electric field, and 3) the Stern layer energy density depend on externally applied potential would add new fundamental insights into our molecular understanding of electrochemical water oxidation. As we will show below, these three properties are readily accessible via the total interfacial potential, Φ_{tot}, and the second-order nonlinear susceptibility, $\chi^{(2)}$, which we demonstrate here are both encoded in the

experimental observables, namely the amplitude and phase of the second harmonic generation (SHG) response.

Prior nonlinear optical studies of electrode:electrolyte interfaces have largely been based on SHG intensity measurements (see Gruen's (*20*) and Nagy and Roy's (*21*) pioneering work on nickel electrodes). These studies hark back to nonlinear electroreflectance studies from silver electrodes (please see Supplementary Information Note S1) (*22-24*). Recent approaches have focused on potential-of-zero charge quantifications via SHG amplitude and phase measurements on a platinum electrode (*9*). We now use optically transparent thin nickel nanolayers for which we quantify the Stern layer structure, the interfacial field, and the Stern layer energy density via $\Phi(0)_{tot}$ and $\chi^{(2)}$.

In the experiments, we begin with a ten-nanometer thin nickel layer (5.1 Å ± 0.5 Å rms roughness) prepared by physical vapor deposition on a glass microscope slide that is subsequently placed into a custom-designed spectro-electrochemical cell (please see Supplementary Information Fig. S1a, and Methods section) connected to an electrochemical workstation. Probing with a femtosecond laser oscillator (80 fs, 1034 nm, 75.5 MHz) and employing single photon counting, we record the SHG intensity simultaneously with the current density as a function of applied potential at pH 13 (as well as pH 7, 9, and 11) and 1 M ionic strength ($NaClO_4$ as well as alkali chlorides). The SHG intensity is quadratic in input power (Supplementary Information Fig. S1b). We find SHG intensity minima that precede the peak potentials of the well-known Ni^{2+}/Ni^{3+} redox pair (Fig. 1a), which follows the expected $(\text{scan rate})^{1/2}$ dependence (Supplementary Information Figure S2c-d) (*25*).

To obtain the SHG amplitude and the absolute phase, we record SHG interference patterns generated by beating the SHG signals from two sources against one another (Fig. 1b): source 1 is

the electrode:electrolyte interface (producing the "signal") and source 2 is a 50 μm thin piece of z-cut α-quartz wafer (producing the local oscillator, "LO") (*26*). The sample and the α-quartz wafer bracket a phase shifting unit consisting of a 1 mm thin fused silica plate mounted on a computerized rotating stage. Collecting the SHG intensity as a function of the rotational angle of the phase shifting unit produces signal + LO interference fringes that whose amplitudes and phases change as we vary the applied potential between -0.5 V and +0.9 V vs Ag/AgCl (Fig. 1c). At each applied potential, the SHG amplitude and phase are obtained through a custom fit function (please see Supplementary Information Note S2).

Using the SHG amplitude and phase we estimate the total interfacial potential, $\Phi(0)_{tot}$, and the second-order nonlinear susceptibility, $\chi^{(2)}$. Using air as opposed to electrolyte, we first obtain the absolute zero phase from the uncoated portion of a glass microscope slide having one half coated with 10 nm nickel and then move the sample cell over by a few millimeters to determine the phase difference of the glass:air vs nickel:air interface to be = -76° ± 19° (standard deviation obtained from Gaussian histogram analysis of 15 electrodes, please see Supplementary Information Methods and Fig. S3a). We then add electrolyte, determine the phase difference of the nickel:air vs nickel:electrolyte interface to be 4° ± 18°, and obtain the point estimates (and associated uncertainties) for the SHG signal phase, φ_{sig} , at a given applied potential, Φ, from $\varphi_{sig} = \varphi_{fit,\Phi} - \varphi_{fit,OCP} - (76° \pm 19°)$. We then normalize the SHG amplitude to the amplitude obtained at OCP. Fig. 2a shows that φ_{sig} decreases with increasing applied potential in a sigmoidal fashion, with a total phase change relative to OCP of -90° at +0.9V applied. On the reverse scan, the phase advances back to 0°. The amplitude goes through minima at the applied potentials that coincide with the SHG intensity minima seen in Fig. 1a. The experiment reproduces reasonably well over seven different electrodes (Supplementary Fig. S3b). We calibrate the SHG response from our

optical window against the second-order nonlinear susceptibility of another z-cut α-quartz piece put in place of the electrolyte solution (*26, 27*), accounting for the normalization factor at OCP, the Fresnel coefficients, and the wave vector mismatch in our experimental geometry (please see Supplementary Information Fig. S5 and Note S3). We then expand an optical model for quantifying $\Phi(0)_{tot}$ and $\chi^{(2)}$ from the SHG amplitude and phase measured at silica:water interfaces for high ionic strength (*26*) to include the metal-specific contributions to the second-order nonlinear susceptibility discussed earlier by Guyot-Sionnest et al. (for Ag) (*28*) and Nagy and Roy (for Ni) (*21*). We obtain the following expression for the total potential drop across the electrode:electrolyte interface (see Supplementary Information Note S4):

$$\Phi(0)_{tot} = -\frac{C \cdot E_{sig,norm}\{5 \cdot cos(\varphi_{sig}) + sin(\varphi_{sig})\}}{(5+1.5)\chi^{(3)}_{water}} \qquad (1)$$

Here, C is the calibration factor that also accounts for OCP normalization of the measured SHG intensities and the Fresnel coefficients (C=3.1 x 10^{-22} m^2V^{-1} in our case, please see Supplementary Information Note S3), $E_{sig,norm}$ is the measured SHG amplitude normalized to the value obtained at OCP (the condition at which we calibrate to quartz, see Supplementary Information Note S3), φ_{sig} is the phase relative to the zero phase from the glass:air interface, and $\chi^{(3)}_{water}$ is the third-order nonlinear susceptibility of the diffuse layer (1x10^{-21} m^2V^{-2} from experiment and theory) (*27, 29*), which is invariant with ionic strength, pH, and surface composition (*30*). Eqn. 1 accounts for the *ca*. 5x larger nonlinear optical response we obtain from the nickel nanolayer when compared to a fused silica window, both at pH 13 and 1 M ionic strength. This experimentally determined factor of 5 is in excellent agreement with the computed factor of 4.5 in eqn. 7 of Nagy and Roy and the 1/2 term in eqn. 1 of Guyot-Sionnest et al. that account for metals' bulk magnetic dipole contribution to $\chi^{(2)}$ (*21, 28*). With eqn. 1 establishing $\Phi(0)_{tot}$, the second-order nonlinear susceptibility is given by (see Supplementary Information Notes S4 and S5):

$$\chi^{(2)} = -\left\{C \cdot E_{sig,norm} sin(\varphi_{sig}) + 1.5 \cdot \Phi(0)_{tot} \cdot \chi^{(3)}_{water}\right\}/5 \qquad (2)$$

Fig. 2b shows the second-order nonlinear susceptibility and the total interfacial potential as a function of externally applied potential. From -0.4 V applied to zero V applied, the total surface potential is near zero mV (± 100 mV from the -60° to -100° range in the phase relative to that of the glass:air interface), consistent with slight negative ζ-potentials at pH 11 and 12.5 of -12 mV and -15 mV, respectively, in 0.1 M $NaNO_3$ (points of zero charge of nickel oxides are at or below pH 11) (*31-33*). We note that the total potential is sum of the Gouy-Chapman-Stern potential associated with the mobile charges (ions) and the contributions from the immobile charges (electrons bound to the molecules and ions), like from dipoles and quadrupoles (*34*). The total potential increases with increasingly positive applied potential until it plateaus near +0.8 V (±0.2 V uncertainty from the replicate electrode measurements, Fig. S3c) at an applied potential of +0.9 V. We note that the absolute potential at an electrode:electrolyte interface cannot be measured using electrochemical means, which only provides the potential difference between two electrodes. The optical approach here does provide the total potential from a single electrode:electrolyte interface, similar to what is in principle possible with (significantly slower) X-ray spectroscopic or electrical impedance measurements on field effect transistors (*35-40*).

Fig. 2b also shows that at OCP, $\chi^{(2)}_{OCP}$ is ~1.1 x 10^{-22} m^2V^{-1}. This non-zero value is attributed to the net aligned dipoles from the interfacial NiOH, NiO^-, and $NiOH_2^+$ groups. Its positive value indicates a net "up" orientation of the interfacial dipoles, i.e. the positive end (Ni^{2+}) pointing into the electrode and the negative end (OH, O^-, or OH_2^+) pointing into the electrolyte. This interpretation is consistent with SHG results from colloidal (*29*) and macroscopically flat (*26*) surfaces showing that positively (*resp.*, negatively) signed values of $\chi^{(2)}$ correspond to water dipoles pointing their negative end (oxygen) away from (*resp.*, towards) the surface. Fig. 2b

indicates that the second-order nonlinear susceptibility becomes smaller in magnitude as the applied potential becomes more positive, and that it crosses zero to become negatively signed at +0.4 V (resp., 0.2 V) applied potential on the forward (resp., reverse) scan, just where the SHG intensities goes through their minima (Fig. 1a). At +0.8 V applied, $\chi^{(2)}$ approaches -1.6 x 10^{-22} x 10^{-22} to -3.1 x 10^{-22} x 10^{-22} m^2V^{-1}, about two times larger in magnitude, albeit oppositely signed, when compared to the value at OCP. Supplementary Fig. S3c shows that the $\chi^{(2)}$ and $\Phi(0)_{tot}$ estimates reproduce reasonably well over seven different electrodes, while Supplementary Fig. S3d shows no apparent pH dependence of the $\chi^{(2)}$ vs applied potential response between pH 13 and 7, while the $\Phi(0)_{tot}$ estimates increase to slightly over 1V at the highest positive potential applied, with a pH dependence of (-0.09 ± 0.04) V pH^{-1}, encompassing the theoretical 0.059 V pH^{-1} Nernst slope at room temperature.

As the interfacial NiOH, NiO^-, and $NiOH_2^+$ groups cannot flip their net orientation, we subtract $\chi^{(2)}_{OCP}$ (1.1 x 10^{-22} x 10^{-22} m^2V^{-1}) from the $\chi^{(2)}$ values obtained at each applied potential to compute the change in the second-order nonlinear susceptibility, $\Delta\chi^{(2)}$. The aim is to estimate the $\chi^{(2)}$ contribution from the mobile Stern lay water molecules, which can change their orientation distribution in response to the applied potential. When $\Phi(0)_{tot}$ is zero, we find that $\Delta\chi^{(2)}$ is near zero (Fig. 2c), which indicates a largely isotropic arrangement of the Stern layer water molecules, in which an approximately equal number of interfacial water molecules point their dipole moments up vs down or are all fully disordered. In other words, $\mathcal{N}\cdot\langle\alpha^{(2)}\rangle=0$, where $\mathcal{N}$ is the total number of Stern layer water molecules and $\cdot\langle\alpha^{(2)}\rangle$ is water's orientationally averaged molecular hyperpolarizability), consistent with the small negative ζ-potential at pH 12 (*31*).

We then proceeded to estimate the number of water molecules that flip their dipole orientations. To this end, we employ the molecular hyperpolarizability for a liquid water model

estimated by Gubskaya and Kusalik at the MP2 and MP4 level of theory ($\alpha^{(2)}$=5.3 x 10^{-52} C m^3V^{-2}) (*41*). This value was used recently by the Roke group (*29*) to estimate the non-resonant third-order nonlinear susceptibility, $\chi^{(3)}$, of liquid water, which is in good agreement with the experimental value reported by the Wen group (*27*). Dividing the $\Delta\chi^{(2)}$ values shown in Fig. 2c by $\alpha^{(2)}$ and multiplying by a Stern layer water permittivity estimate of 1.9 (the mean of ε=1.77, the square of water's index of refraction at 515 nm, and ε=2.0, from recent experiments (*42*)) and the vacuum permittivity, ε_0, according to $\mathcal{N}_{\downarrow}$= $|\Delta\chi^{(2)}|\cdot\varepsilon\varepsilon_0/(10^4\ cm^2\ m^{-2}\cdot\alpha^{(2)})$ yields the number of water molecules per cm^2 that point their oxygen atoms down towards the electrode. Fig. 2d shows that at the most positive applied potential (+0.9 V), ca. 1.1 x 10^{15} water molecules per square cm have a net orientation with their oxygen atoms pointing towards the electrode. Larger values for $\mathcal{N}_{\downarrow}$ would arise from larger values for the Stern layer relative permittivity. In addition, the angular orientation distribution of the Stern layer water molecules relative to the surface normal is not known and could very well be multimodal. Yet, under the s-in/p-out polarization combination employed here, our estimate for $\mathcal{N}_{\downarrow, max}$=1.1 x 10^{15} cm^{-2} matches the geometric number density of water molecules on the surface of a 1 cm^3 cube of liquid water at standard temperature and pressure (1 x 10^{15} cm^{-2}), i.e. one water monolayer, consistent with the notion that the experiments report, to leading order, on the surface normal projection of the dipole orientations.

In contrast to the sigmoidal dependence of the number of net-aligned Stern layer water molecules on applied potential shown in Fig. 2d, the right-hand axis of Fig. 2c shows that water flipping is linear in the total potential across the electrode:electrolyte interface. Flipping all the Stern layer water molecules requires a field of close to -1 x 10^7 V cm^{-1} (top x-axis in Fig. 2c) – an experimental match with estimates from classic electrochemical textbooks (*43*), now obtained using purely optical means. To investigate the energetics associated with Stern layer water

flipping, we computed the total energy density in the Stern layer by multiplying the total potential by the elemental charge and the number of oriented Stern layer water molecules according to $E_{flip} = \Phi_{tot} \cdot e \cdot \mathcal{N}_{water\downarrow}$, showing a sigmoidal variation with applied potential (Fig. 3a). In contrast, we find a parabolic variation of the Stern layer energy density with $f_\downarrow$, the fraction of Stern layer water molecules pointing their oxygen atoms towards the electrode (Fig. 3b, note that for $f_\downarrow$=0.5, $\mathcal{N}_\downarrow$=0, *i.e.* there is no net order, and for $f_\downarrow$=1.0, $\mathcal{N}_\downarrow = \mathcal{N}_{\downarrow,max}$, i.e. all water molecules have flipped). The experimental results can be interpreted using a 2-dimensional, two-state Ising model in which we express *F*, the Helmholtz free energy mean field solution for the square lattice model (z=4), according to (*44*)

$$F = (\mathcal{N}_\downarrow)^2 J \frac{z}{2} - \beta^{-1} ln\left[cosh\left(\beta \cdot (Jz|\mathcal{N}_\downarrow| + e \cdot \Phi_{tot})\right)\right] \qquad (3)$$

Here, $\mathcal{N}_\downarrow = -3 \times 10^{13} - \Phi_{tot} \times 1 \times 10^{15}$ (the linear least squares fit result of $\mathcal{N}_\downarrow$ vs Φ_{tot}, Fig. 2C), $\beta = (k_B T)^{-1}$ with k_B being the Boltzmann constant, T is the temperature (300K), and *e* is the elementary charge. The model recapitulates the experimental data with a coupling constant, J, of -1×10^{-34} J for the aligned Stern layer water molecules, again using ε=1.9. With z = 6, we find $J = -0.6 \times 10^{-34}$ J best recapitulates the experimental data. These results support the notion that the experiments are largely sensitive to the dipole "up" vs "down" orientations of the Stern layer water molecules. At the highest applied potential, where $\mathcal{N}_\downarrow = \mathcal{N}_{\downarrow,max} = 1 \times 10^{15}$ molecules, the work associated with water flipping corresponds to 80 kJ mol^{-1}, exceeding the cohesive energy of ice by 20 kJ mol^{-1} (*45*). Fig. 3c shows that the water flipping process begins prior to the onset of Faradaic current flow (the nickel oxidation wave at +0.4 V), indicating that the oxygen evolution reaction in this case requires water flipping first, followed by electron transfer.

In conclusion, we report the development of a facile optical readout for estimating the number of Stern layer water molecules that point their electron-rich oxygen atoms towards an

anode as a function of applied potential. We obtain estimates for the total surface potential, the electric field, and the work in the Stern layer under operando electrochemical conditions. At the highest potentials applied (+0.9V vs Ag/AgCl, pH 13), we find 1.1 x 10^{15} water molecules per square centimeter are net aligned oxygen atoms towards the electrode. A two-dimensional Ising model recapitulates the experimental results. Prior to starting the Faradaic process at +0.4 V, the work associated with water flipping is negligible and approximately 2/3 to 3/4 of a monolayer of Stern layer water molecules are already net-aligned with their oxygen atoms pointed towards the electrode. These results indicate that water orientation is a necessary condition for the oxygen evolution reaction to occur in case of the nickel electrodes studied here (Fig. 3d). At +0.6 V applied potential, the Stern layer energy density has increased to match the cohesive energy of liquid water. At ~+0.9 V applied potential, all the Stern layer water molecules ($\mathcal{N}_{\downarrow, max}$= 1.1 x 10^{15} cm^{-2}) have flipped to point their oxygen atoms towards the electrode and the associated Stern layer energy exceeds the cohesive energy of ice by ~20 kJ mol^{-1}.

We expect that our fundamental insights will add to the ongoing rapid development of molecular electrochemistry. Noting that the level of quantification presented here would not be possible with the information and models that have existed until now, the experimental data we present can serve as benchmarks for theoretical models of the electrical double layer and electrochemistry. They establish that the Stern layer water molecules flip prior to the onset of the oxygen evolution reaction and thereby open the possibility to pursue the energy barrier for water flipping as a means for addressing the OER's high overpotential on nickel anodes. Beyond the new physical insights and experimental benchmarks, the ability to 1) count the number of Stern layer water molecules, 2) determine their net absolute orientation, and 3) quantify the electrostatic field and energy density at electrode:electrolyte interfaces under *operando* conditions represents a new

diagnostic toolkit that we envision to help elucidate why the platinum group elements are better water oxidation catalysts when compared to, say, catalysts comprised of earth abundant metals such as nickel or iron, particularly from a perspective of the electron source, i.e. that of the interfacial water molecules. Our new capabilities and insights into solvent structure and energetics should be equally applicable to the ongoing development of synthetic electrochemistry.

References

1. Y. Zhang, H. B. de Aguiar, J. T. Hynes, D. Laage, Water Structure, Dynamics, and Sum-Frequency Generation Spectra at Electrified Graphene Interfaces. *J. Phys. Chem. Lett.* **11**, 624-631 (2020).
2. Water structures on a Pt(111) electrode from ab initio molecular dynamic simulations for a variety of electrochemical conditions. *Phys. Chem. Chem. Phys.* **22**, 10431-10437 (2020).
3. J. Rossmeisl *et al.*, Realistic Cyclic Voltammograms from Ab Initio Simulations in Alkaline and Acidic Electrolytes. *J. Phys. Chem. C* **124**, 20055-20065 (2020).
4. O. M. Magnussen, A. Gross, Toward an Atomic-Scale Understanding of Electrochemical Interface Structure and Dynamics. *J. Am. Chem. Soc.* **141**, 4777-4790 (2019).
5. C. Zhang, J. Hutter, M. Sprik, Coupling of Surface Chemistry and Electric Double Layer at TiO2 Electrochemical Interfaces. *J. Phys. Chem. Lett.* **10**, 3871-3876 (2019).
6. J. Vatamanu, O. Borodin, Ramifications of Water-in-Salt Interfacial Structure at Charged Electrodes for Electrolyte Electrochemical Stability. *J. Phys. Chem. Lett.* **8**, 4362-4367 (2017).
7. Z. Futera, N. J. English, Water Breakup at Fe2O3−Hematite/Water Interfaces: Influence of External Electric Fields from Nonequilibrium Ab Initio Molecular Dynamics. *J. Phys. Chem. Lett.* **12**, 6818-6826 (2021).
8. J. L. Bañuelos *et al.*, Oxide–and Silicate–Water Interfaces and Their Roles in Technology and the Environment. *Chem. Rev.* **123**, 6413-6544 (2023).
9. P. Xu, A. D. von Rueden, R. Schimmenti, M. Mavrikakis, J. Suntivich, Optical method for quantifying the potential of zero charge at the platinum-water electrochemical interface. *Nature Materials* **22**, 503-510 (2023).
10. S. M. Piontek *et al.*, Probing Heterogeneous Charge Distributions at the α-Al2O3(0001)/H2O Interface. *J. Am. Chem. Soc.* **142**, 12096-12105 (2020).
11. A. Ge *et al.*, On the Coupling of Electron Transfer to Proton Transfer at Electrified Interfaces. *J. Am. Chem. Soc.* **142**, 11829-11834 (2020).
12. C.-Y. Li *et al.*, In situ probing electrified interfacial water structures at atomically flat surfaces. *Nature Mat.* **18**, 697-701 (2019).
13. S.-J. Shin *et al.*, On the importance of the electric double layer structure in aqueous electrocatalysis. *Nature Comm.* **13**, 174 (2022).
14. G. Gonella *et al.*, Water at charged interfaces. *Nature Reviews Chemistry* **5**, 466-485 (2021).
15. F. J. Sarabia, P. Sebastián-Pascual, M. T. M. Koper, V. Climent, J. M. Feliuy, Effect of the Interfacial Water Structure on the Hydrogen Evolution Reaction on Pt(111) Modified with Different Nickel Hydroxide Coverages in Alkaline Media. *ACS Appl. Mater. Interfaces* **11**, 613-623 (2019).
16. M. R. Nellist *et al.*, Potential-sensing electrochemical atomic force microscopy for in operando analysis of water-splitting catalysts and interfaces. *Nat. Energy* **3**, 46-52 (2018).
17. Z. Liang, H. S. Ahn, A. J. Bard, A Study of the Mechanism of the Hydrogen Evolution Reaction on Nickel by Surface Interrogation Scanning Electrochemical Microscopy. *J. Am. Chem. Soc.* **139**, 4854-4858 (2017).
18. K.-i. Ataka, T. Yotsuyanagi, M. Osawa, Potential-Dependent Reorientation of Water Molecules at an Electrode/Electrolyte Interface Studied by Surface-Enhanced Infrared Absorption Spectroscopy. *J. Phys. Chem.* **100**, 10664-10672 (1996).

19. F. Song *et al.*, Transition Metal Oxides as Electrocatalysts for the Oxygen Evolution Reaction in Alkaline Solutions: An Application-Inspired Renaissance. *J. Am. Chem. Soc.* **140**, 7748-7759 (2018).
20. B. M. Biwer, M. J. Pellin, M. W. Schauer, D. M. Gruen, Electrochemical and Second Harmonic Generation Investigation of Nickel Corrosion in 0.1 M NaOH. *Surf. Interf. Anal.* **14**, 635-646 (1989).
21. G. Nagy, D. Roy, Surface charge dependence of second harmonic generation from a Ni electrode. *Chem. Phys. Lett.* **214**, 197-202 (1993).
22. C. H. Lee, R. K. Chang, N. Bloembergen, Nonlinear Electroreflectance in Silicon and Silver. *Phys. Rev. Lett.* **18**, 167-170 (1967).
23. G. L. Richmond, Surface second harmonic generation from sulfate ions adsorbed on silver electrodes. *Chem. Phys. Lett.* **106**, 26-29 (1984).
24. R. M. Corn, M. Romagnoli, M. D. Levenson, M. R. Philpott, The Potential Dependence of Surface Plasmon-Enhanced Second-Harmonic Generation at Thin Film Silver Electrodes. *Chem. Phys. Lett.* **106**, 30-35 (1984).
25. M. S. A. Akbari, R. Bagheri, Z. Song, M. M. Najafpour, Oxygen-evolution reaction by nickel/nickel oxide interface in the presence of ferrate (Vi). *Sci. Rep.* **10**, 8757 (2020).
26. E. Ma *et al.*, A New Imaginary Term in the 2nd Order Nonlinear Susceptibility from Charged Interfaces. *J. Phys. Chem. Lett.* **12**, 5649-5659 (2021).
27. L. Dalstein, K.-Y. Chiang, Y.-C. Wen, Direct Quantification of Water Surface Charge by Phase-Sensitive Second Harmonic Spectroscopy. *The Journal of Physical Chemistry Letters* **10**, 5200-5205 (2019).
28. P. Guyot-Sionnest, A. Tadjeddine, A. Liebsch, Electronic Distributions and Nonlinear Optical Response at the Metal-Electrolyte Interface. *Phys. Rev. Lett.* **64**, 1678-1681 (1990).
29. C. Lütgebaucks, G. Gonella, S. Roke, Optical label-free and model-free probe of the surface potential of nanoscale and microscopic objects in aqueous solution. *Phys. Rev. B* **94**, 195410 (2016).
30. Y.-C. Wen *et al.*, Unveiling Microscopic Structures of Charged Water Interfaces by Surface-Specific Vibrational Spectroscopy. *Physical Review Letters* **116**, 016101 (2016).
31. T. Mahmood *et al.*, Comparison of Different Methods for the Point of Zero Charge Determination of NiO. *Industrial & Engineering Chemistry Research* **50**, 10017-10023 (2011).
32. M. Kosmulski, The pH dependent surface charging and points of zero charge. VI. Update. *Journal of Colloid and Interface Science* **426**, 209-212 (2014).
33. P. H. Tewari, A. B. Campbell, Temperature Dependenceof Pointof Zero Chargeof Cobalt and Nickel Oxidesand Hydroxides. *J. Coll. Int. Sci.* **55**, 531-539 (1976).
34. A. L. Olson, A. O. Alghamdi, F. M. Geiger, NaCl, MgCl2, and AlCl3 Surface Coverages on Fused Silica and Adsorption Free Energies at pH 4 From Nonlinear Optics, chemRxiv 10.26434/chemrxiv-2024-6t3wz. (2024).
35. L. Bousse, Single electrode potentials related to flat-band voltage measurements on EOS and MOS structures. *J. Chem. Phys.* **76**, 5128-5133 (1982).
36. L. Bousse, N. F. De Rooij, P. Bergveld, Operation of Chemically Sensitive Field-Effect Sensors As a Function of the Insulator-Electrolyte Interface. *IEEE Trans. Electron Devices* **ED-30**, 1263-1270 (1983).

37. J. L. Diot, J. Joseph, J. R. Martin, P. Clechet, pH Dependence of the Si/SiO2 Interface State Density for EOS Systems: Quasi-Static and AC Conductance Methods. *J. Electroanal. Chem.* **193**, 75-88 (1985).
38. M. A. Brown *et al.*, Determination of Surface Potential and Electrical Double-Layer Structure at the Aqueous Electrolyte-Nanoparticle Interface. *Phys. Rev. X* **6**, 011007 (2016).
39. M. A. Brown, G. V. Bossa, S. May, Emergence of a Stern Layer from the Incorporation of Hydration Interactions into the Gouy–Chapman Model of the Electrical Double Layer. *Langmuir* **31**, 11477-11483 (2015).
40. M. A. Brown, A. Goel, Z. Abbas, Effect of Electrolyte Concentration on the Stern Layer Thickness at a Charged Interface. *Angewandte Chemie International Edition* **55**, 3790-3794 (2016).
41. A. V. Gubskaya, P. G. Kusalik, The multipole polarizabilities and hyperpolarizabilities of the water molecule in liquid state: an ab initio study. *Mol. Phys.* **99**, 1107-1120 (2001).
42. L. Fumagalli *et al.*, Anomalously low dielectric constant of confined water. *Science* **360**, 1339-1342 (2018).
43. A. J. Bard, L. R. Faulkner, *Electrochemical Methods: Fundamentals and Applications*. (John Wiley and Sons, New York, ed. 2nd, 2000).
44. A. Codello, Please see Chapter 5, Ising Model and Phase Transitions, in https://universalitylectures.wordpress.com. (2013).
45. V. F. Petrenko, R. W. Whitworth, *Physics of Ice*. (Oxford University Press, New York, 1999).

Acknowledgments. RS and FMG acknowledge US National Science Foundation grant CHE-2153191. This work was also supported the Air Force Office of Scientific Research (FA9550-16-1-0379, partial funding for the electrochemical cell design and manufacturing), the Department of Energy (DE-SC0023342, partial funding for the oscillator), and the Army Research Office/Defense Advanced Research Program Agency (W911NF1910361/75506-CH-DRP, funding the PVD instrumentation).

Contributions. FMG conceived of the idea. RS and FMG designed and carried out the experiments, analyzed the data, and wrote the manuscript.

Corresponding Author. E-mail: f-geiger@northwestern.edu

Ethics Declaration. The authors declare no competing interests.

Data Availability. The data supporting the findings of this study are available within the main text and the Supplementary Information and upon request from the corresponding author.

Supplementary Materials

Materials and Methods

Supplementary Notes S1-S5.

Figs. S1 to S10

References

Fig. 1

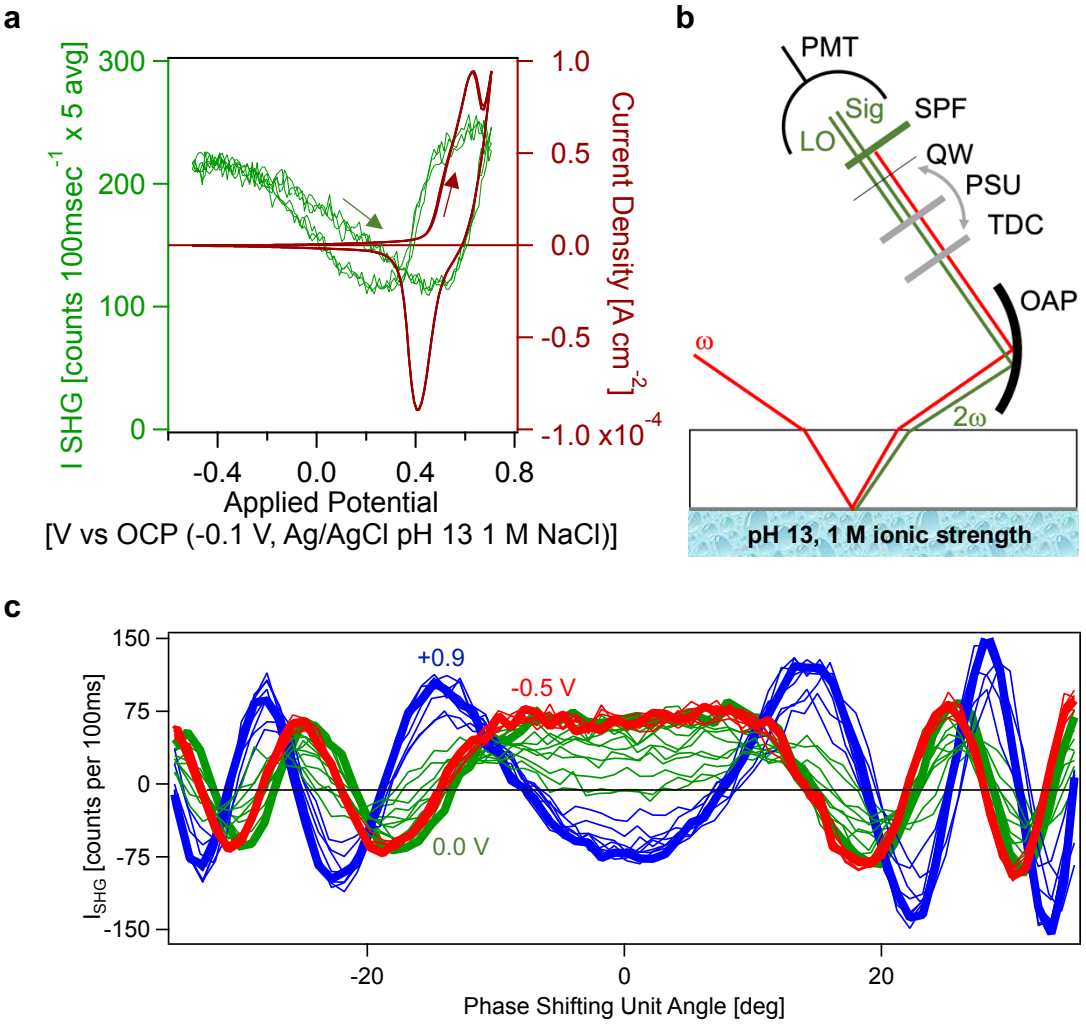

Fig. 1 a) SHG intensity (left ordinate) and current density (right ordinate) recorded as a function of applied potential during three replicate cyclic voltammograms collected at 20 mV s^{-1}. **b**) Top view of the beam path for the SHG signal and local oscillator pair. OAP=off-axis parabolic mirror, TDC=time-delay compensator, PSU=motorized phase shifting unit, QW=quartz wafer, Sig=signal, LO=local oscillator, SPF=short pass filter, PMT=photomultiplier tube. Beams offset for clarity. **c**) Interference fringes recorded from the electrode:electrolyte interface as a function of applied potential, with 1 M $NaClO_4$ and pH 13, adjusted using NaOH.

Fig. 2

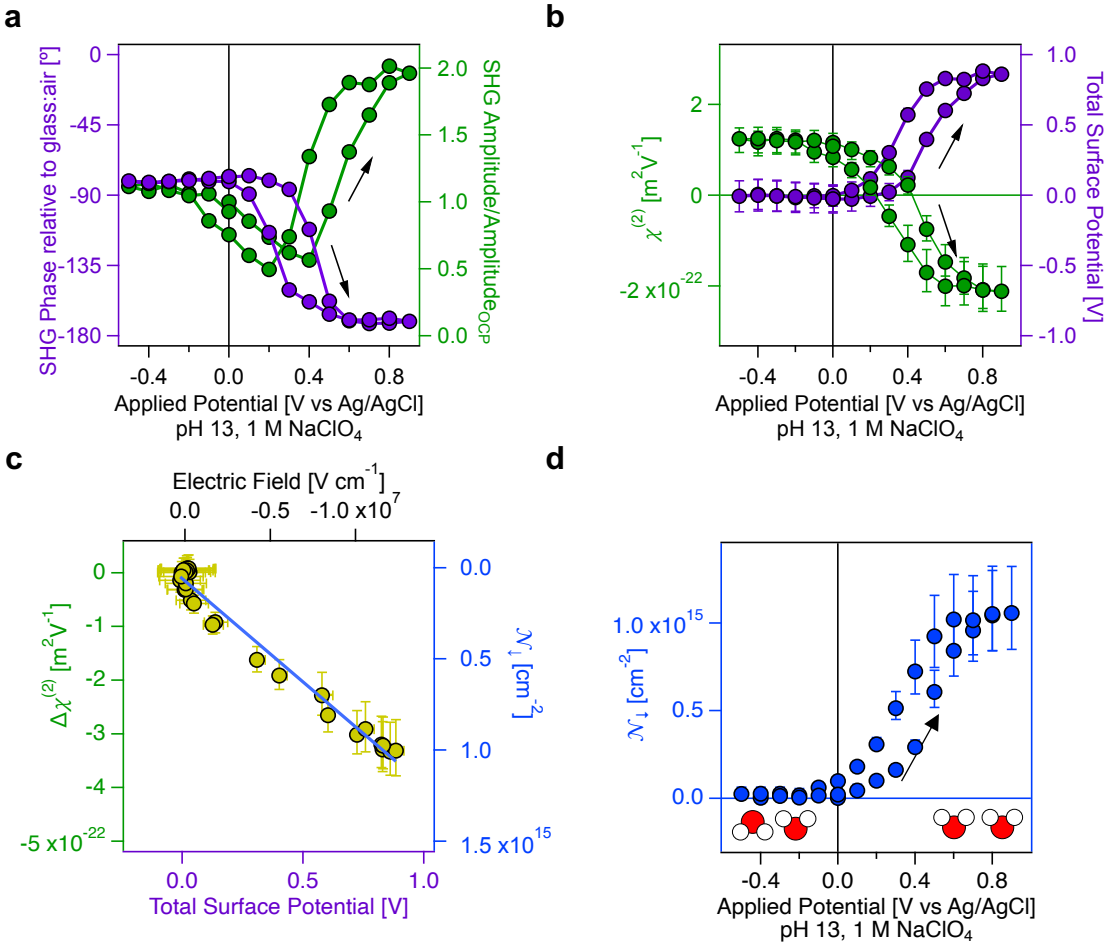

Fig. 2. **a**) SHG Phase (left ordinate) and amplitude (right ordinate) as a function of applied potential. Uncertainties in the fit parameters are 1.5° in the phase and 3% in the intensity and are obscured by the circle diameter. **b**) Second order nonlinear susceptibility (left ordinate) and total potential (right ordinate) as a function of applied potential. Uncertainties from propagating +/- 19° phase uncertainty. **c**) Second order nonlinear susceptibility at a given total surface potential minus the second order nonlinear susceptibility obtained at open circuit potential (left ordinate) and number of net-aligned Stern layer water molecules (right ordinate) as a function of total surface potential (lower abscissa) and electric field (upper abscissa). **d**) Number of net-aligned Stern layer water molecules pointing their oxygen atoms towards the electrode as a function of applied potential.

Fig. 3

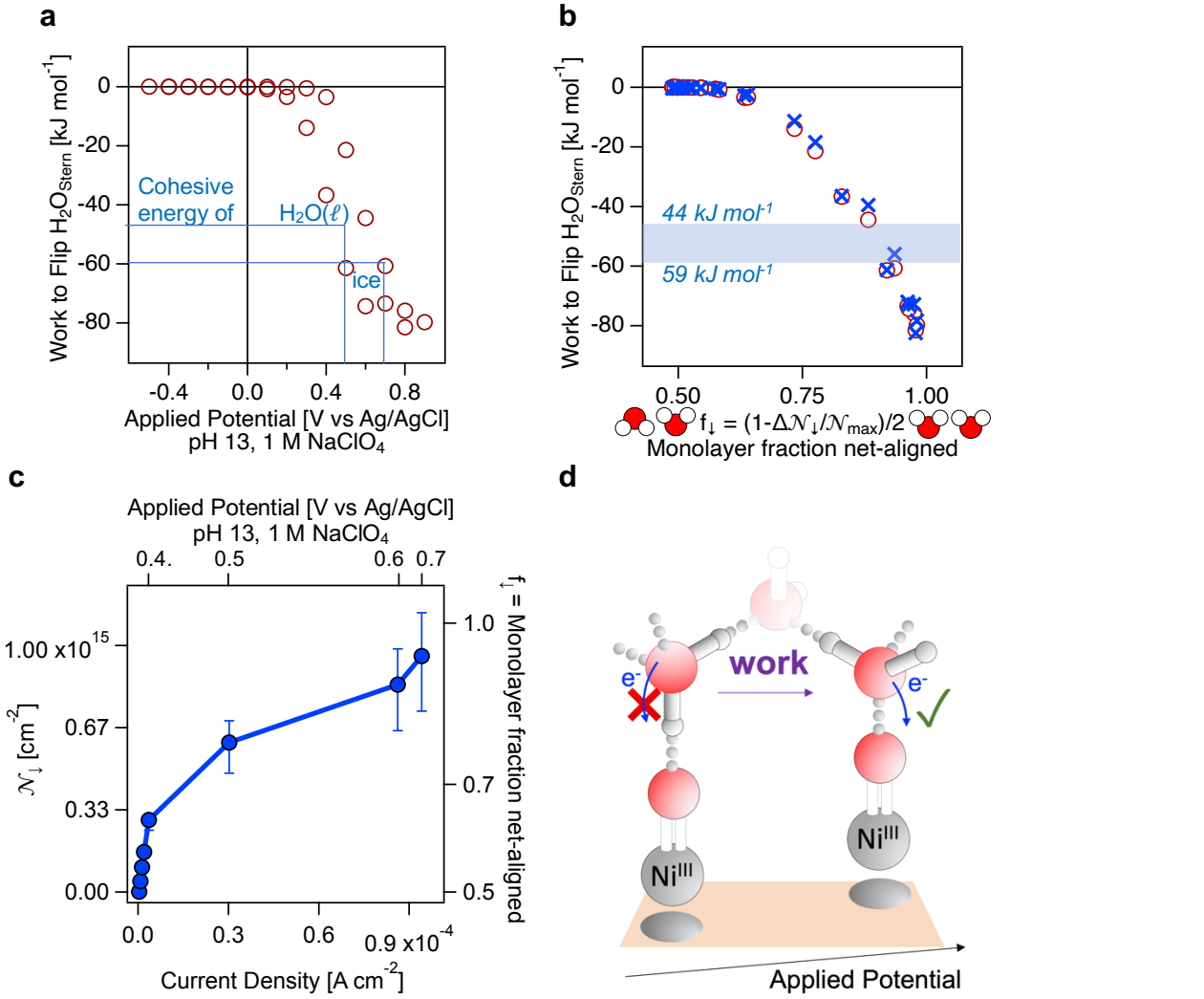

Fig. 3. a) Work associated with Stern layer water flipping as a function of applied potential. The cohesive energies of liquid water and ice are indicated. **b**) Work associated with Stern layer water flipping as a function of the fraction of water molecules having a net-orientation with their oxygen atoms pointed towards the electrode. Upper and lower bounds of shaded area indicate range of cohesive energies of liquid water and ice, respectively. Blue crosses indicate 2D-Ising model with J=-1 x 10^{-34} J. **c**) Number (left ordinate) and fraction (right ordinate) of net-aligned water molecules pointing their oxygen atoms towards the electrode as a function of measured current density (bottom abscissa) and applied potential (top abscissa). **d**) Cartoon of water flipping concept.

Supporting Information for

Quantifying Stern Layer Water Alignment Prior to and During the Oxygen Evolution Reaction

Raiden Speelman and Franz M. Geiger*

Department of Chemistry, Northwestern University,

2145 Sheridan Road, Evanston, IL 60660, USA

*f-geiger@northwestern.edu

The Supporting Information includes experimental and procedural details as well as nanolayer characterization and additional information, as referred to in the main text.

Methods. The electrochemical workstation is a Metrohm Autolab model (PGSTAT302N with a SCAN250 true linear analog sweep module). The nickel (working), counter (platinum), and reference (Ag:AgCl) electrodes in contact with aqueous electrolyte (pH 13 and 1 M $NaClO_4$). FKM O-rings are used for sealing the spectro-electrochemical cell housing the electrodes, which is unstirred and consists of a double-paned custom-designed assembly (redox.me) manufactured from PEEK (please see Supplementary Information Fig. S1a). The open circuit potential is measured before each electrochemical experiment to be -0.094V +/-0.007 V (vs Ag/AgCl, at pH 13, 1 M ionic strength, average of 33 measurements). One window consists of a standard 1 inch x 3 inch VWR microscope glass slide onto which a ten-nm thin nickel nanolayer is deposited from nickel sources having a purity of 99.98 (Kurt J. Lesker) using a physical vapor deposition method that minimizes the presence of low-boiling point impurities (K, Ca, Mg) in the deposited nanolayer (*1*). The second window is a fused silica window that allows for the incident laser pulses at the fundamental frequency to exit the electrochemical assembly towards a beam stop.

X-ray photoelectron spectroscopy shows the presence of nickel oxide on the electrode surface (*1*). The nickel oxidation and reduction waves integrate to between 1.1 x 10^{-3} A s and 1.3

x 10^{-3} A s, corresponding to 7 x 10^{15} to 8 x 10^{15} electrons transferred (comparable to undoped NiO electrodes) (*2*) and thus 7 to 8 monolayer equivalents of Ni^{2+}/Ni^{3+}, or an electrochemically active oxide thickness of 1.4 to 1.6 nm, assuming a Ni-O bond length of 2Å. This oxide thickness is on the order of what we reported earlier from atom probe tomography for iron nanolayers (*3*) prepared using the same low-impurity PVD method that is employed here for the nickel nanolayers. Atomic force microscopy (Bruker) shows the electrodes to have a root mean square roughness of 5.1 Å ± 0.5 Å over 1 x 1 μm^2 and 300 x 300 nm^2 areas before and after the electrochemical measurements (please see Supplementary Information Figs S6), matching that of the substrates onto which they are deposited. Optical imaging shows no pinholes, but they are found on rare occasions in SEM images (please see Supplementary Information Figs S7). Water contact angles recorded immediately after nanolayer formation are <10° but increase to over 50° when the nanolayers are left in ambient laboratory air for several hundred hours (please see Supplementary Information Figs S8), indicating hydrocarbon buildup. We therefore subject each electrode, once mounted in the e-chem cell, to replicate cyclic voltammograms (-0.3 V to +0.8V) until they are indistinguishable from one another, typically five to ten cycles.

We direct 0.2 W from a LightConversion Flint oscillator (model FL1-02) producing 80 femtosecond pulses at 1034 nm at a 75.5 MHz repetition rate onto the electrode:electrolyte interface using a defocused (-1 cm) 10 cm lens (spot size *ca*. 100 μm diameter) and block the reflected fundamental light from the external air:window interface. We direct the SHG signal pulses along with the reflected fundamental pulses from the electrode:electrolyte interface towards an off-axis parabolic mirror and a 0.5 mm thin uncoated calcite time delay compensator (Newlight Photonics, CAL12050-A) to account for spatial and temporal dispersion at the detector, as described in our earlier work (*4*). The fundamental and SHG pulses are then sent through a 1 mm thin fused silica phase shifting unit (Edmund Optics) on a rotating stage (Standa model 8MR174-

11), and then through a 50 um thin z-cut a-quartz wafer (Precision Micro-Optics PWQB-368252) producing the local oscillator (LO). The SHG pulse pair (signal+LO) then interferes at the detector (Hamamatsu H8259-01) as a function of the phase shifting unit (PSU) angle.

At each PSU angle, we collect the SHG signal at 100 ms acquisition time for 5, 10, or 20 seconds, so it takes as little as a minute to record one fringe and reset the PSU motor position. We employ an applied voltage staircase in 100 mV steps that parks at a given voltage for the time required to record three fringes, of which we employ the third for fitting. We then obtain the signal (i.e., electrode:electrolyte interface) amplitude and phase from a trigonometric fit function detailed in Supporting Information Section S2.

Replicate measurements of the SHG phase in air were performed using various laser spot positions on a given glass slide or nickel electrode with 15 in different electrodes so as to account for variations in the measurements that come along with slight variations in how the sample cell is assembled and mounted between replicates/trials (please see Supplementary Information Fig. S3a). We first obtain the absolute zero phase from the uncoated portion of a glass microscope slide having one half coated with 10 nm nickel and then move the sample cell over by a few millimeters to determine the fitted phase of the metal nanolayer. We mount the slide in the electrochemical cell and contact it with air (no electrolyte present). The uncoated part of the glass slide is fully transparent at the wavelengths employed here, not birefringent, and the surface potential is zero, so that the SHG response is purely real, *i.e.* $E_{SHG,glass:air}\, e^{i\varphi_{,glass:air}} =$ real, with $\varphi_{,glass:air}$ =0°. We collect a fringe on the uncoated glass side and obtain a fitted phase, φ_{fit}, using a trigonometric fit function detailed in Supplementary Information Section S2. This fitted phase is the offset we apply to the phases we obtain when moving the cell such that the laser beam hits the nickel nanolayer. Replicate measurements obtained by assembling and reassembling 15 glass/nickel slides in our cell show $\varphi_{nickel:air}$ - $\varphi_{glass:air}$ = -76° ± 19° (standard deviation obtained from Gaussian

histogram analysis, please see Supplementary Information Fig. S3a), with the upper limit close to the 90° phase shift reported for non-resonant sum frequency signals from gold (*5*). Keeping the laser focused on the nickel portion of the cell, we fill the cell with electrolyte using a peristaltic pump and obtain $\varphi_{nickel:air}$ - $\varphi_{nickel:electrolyte}$ = 4° ± 18° (again with 15 replicates) at open circuit potential (OCP, -0.1 V vs Ag/AgCl in our cell, please see Supplementary Information Fig. S4). Given these results, we first offset the fitted phase obtained at each applied potential by the one obtained at OCP. We then subtract another 57° to 95° to estimate the absolute phase from the electrode:electrolyte interface under applied potential.

Attempts to obtain the absolute phase from a z-cut α-quartz crystal aligned along the x-axis (*6, 7*) and pressed against a glass slide in our electrochemical cell were unsuccessful. While the interference fringes are readily observed, the fitted phases vary tens to 100s of degrees as we move from one sample spot to the next, or from one sample assembly to the next. The problem persists with index matching fluid. We attribute this result to imperfect flatness and the resulting gap between the two solids and conclude that the air-first and electrolyte-second approach is a reliable means for the phase estimate.

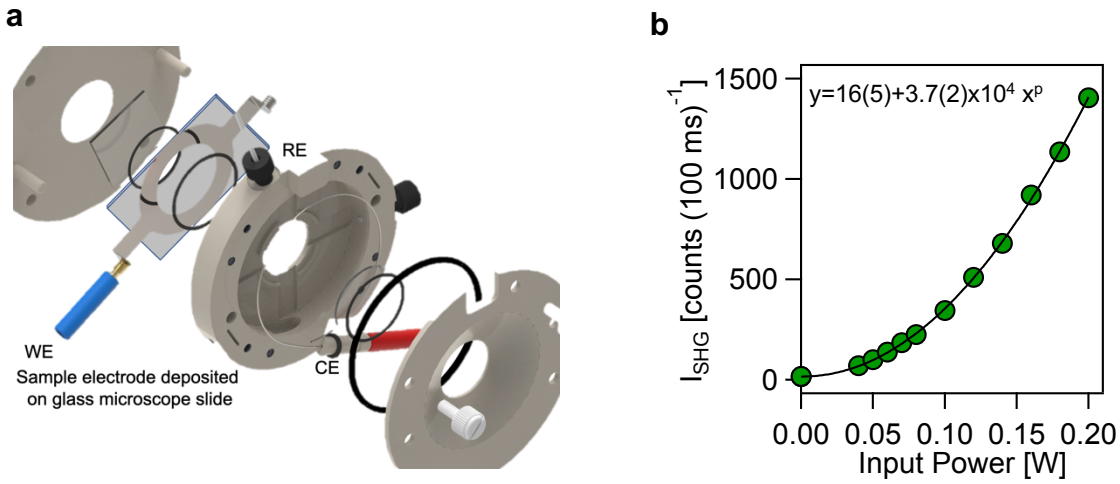

Fig. S1. a) Detailed view of the electrochemical cell used in the experiments. WE=working electrode, CE=platinum counter electrode, RE=Ag/AgCl reference electrode. **b**) SHG Signal intensity vs incident input power and fit to a power function producing an estimate for p of 2.04 ± 0.03.

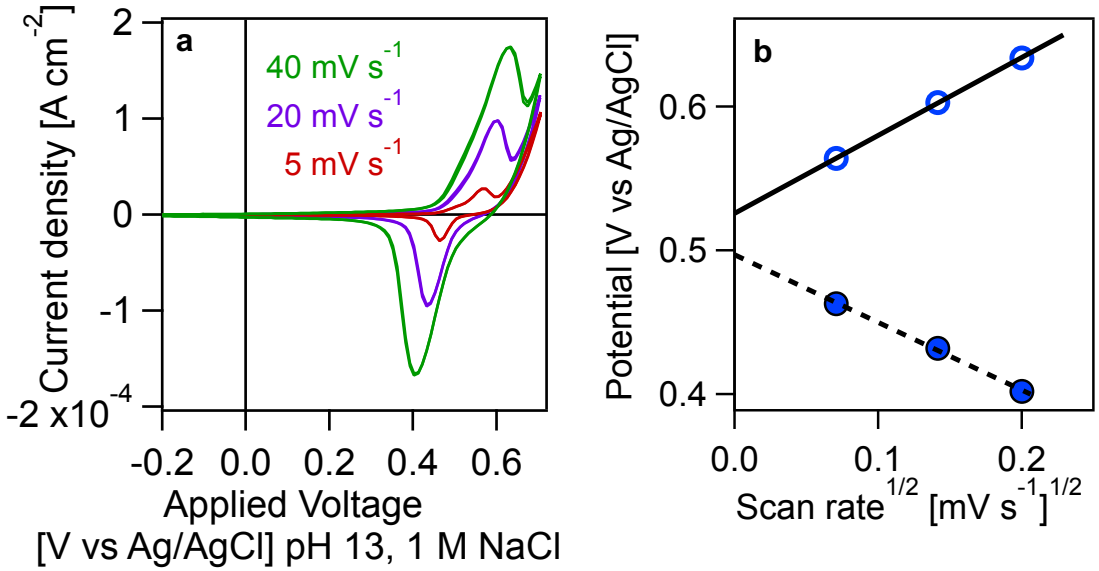

Fig. S2. a) Cyclic voltammograms recorded with indicated scan rates. **b**) Ni(II)/Ni(III) Oxidation peak potential vs (scan rate)$^{1/2}$ and linear fits (y=a+b*x) where a=0.5259 ± 0.0009 V and 0.497 ± 0.003 V and b=0.542 ± 0.006 mV$^{1/2}$s$^{1/2}$ and -0.47 ± 0.02 mV$^{1/2}$s$^{1/2}$ for the anodic and the cathodic peaks, respectively.

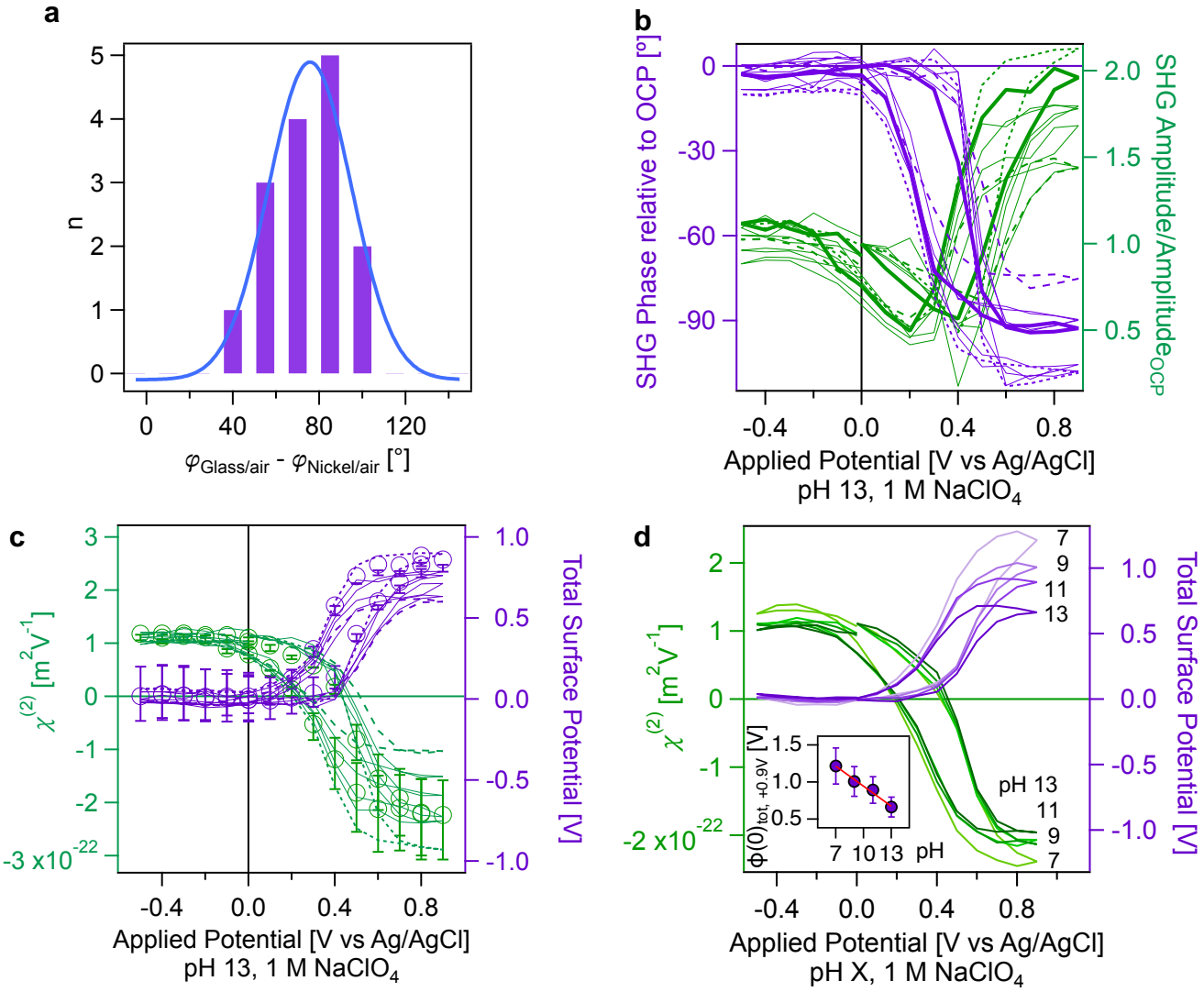

Fig. S3. a) Histogram of 15 measurements of $\varphi_{glass:air}$ - $\varphi_{nickel:air}$ and Gaussian fit having a mean of 76° and a standard deviation of 19°. **b**) SHG Amplitude and phase obtained from 7 different electrodes. As 3 examples, the thick, dash ed, and dotted lines m ark the amplitude and phase pairs obtained from a given electrode. **c**) Same as in b), but for $\chi^{(2)}$ and $\Phi(0)_{tot}$. The $\chi^{(2)}$ $\Phi(0)_{tot}$ pair from the main text is given as well (empty circles). **d**) Second-order nonlinear susceptibility and total interfacial potential as a function of applied potential for electrolyte held at pH 7, 9, 11, and 13, indicated by increasingly darker line color. All pH runs performed on the same electrode; pH was changed using a peristaltic pump. Inset: $\Phi(0)_{tot}$ at +0.9V applied vs pH, and slope of 0.09 ±0.04 V pH^{-1} from weighted linear least squares fit (solid line).

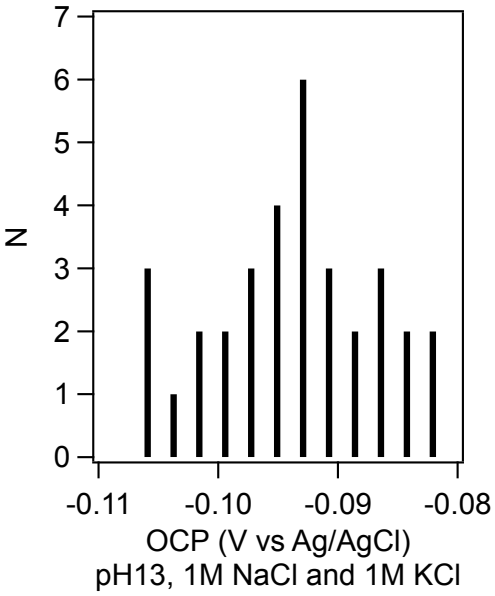

Fig. S4. Histogram of open circuit potential from 33 replicates before and after CV sweeps.

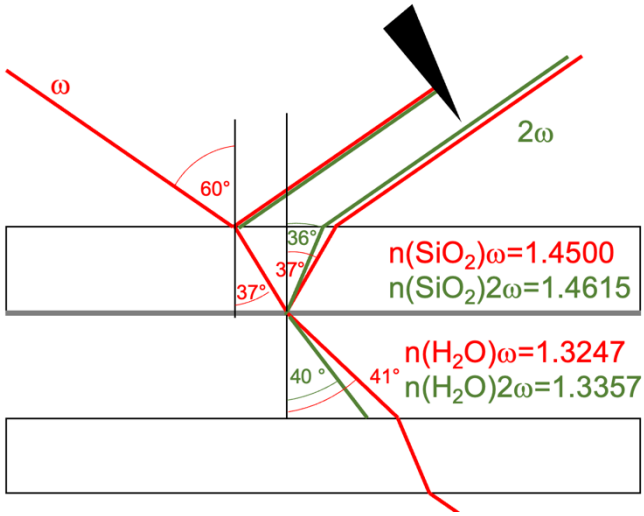

Fig. S5. Top view of the optical beam paths in the electrochemical cell. The 10 nm-thin nickel electrode is indicated as the thin grey line at the bottom of the top window. A piece of anodized aluminum blocks the reflected fundamental and second harmonic from the top surface of the top window.

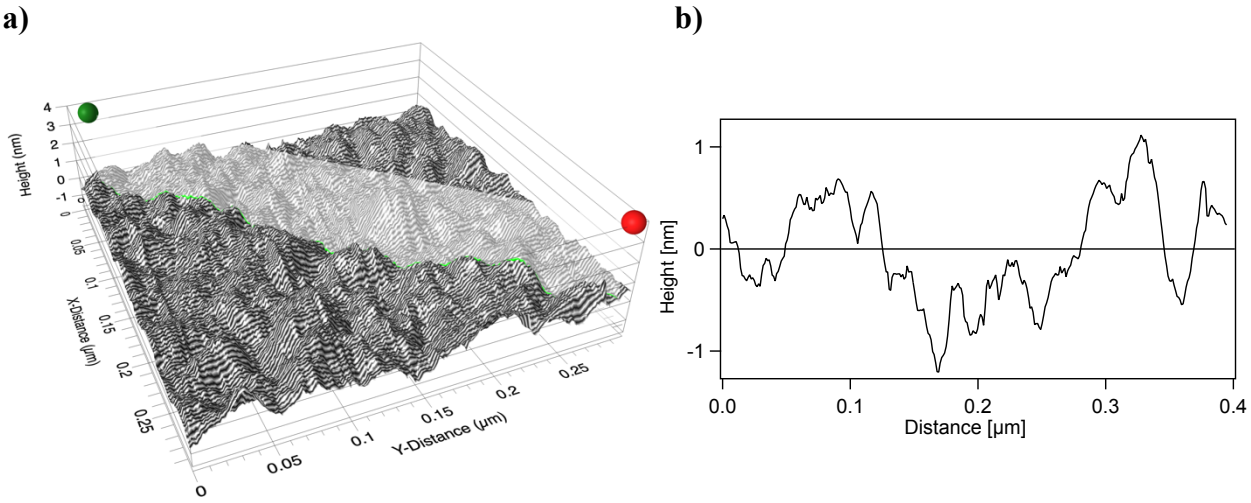

Fig. S6. a) Atomic force microscope image (Bruker Icon, tapping-in-air mode, 2 Hz scan rate) of a 10 nm nickel electrode on a VWR glass microscope slide after cyclic voltammetry. **b**) Line profile along the diagonal indicated in **a**).

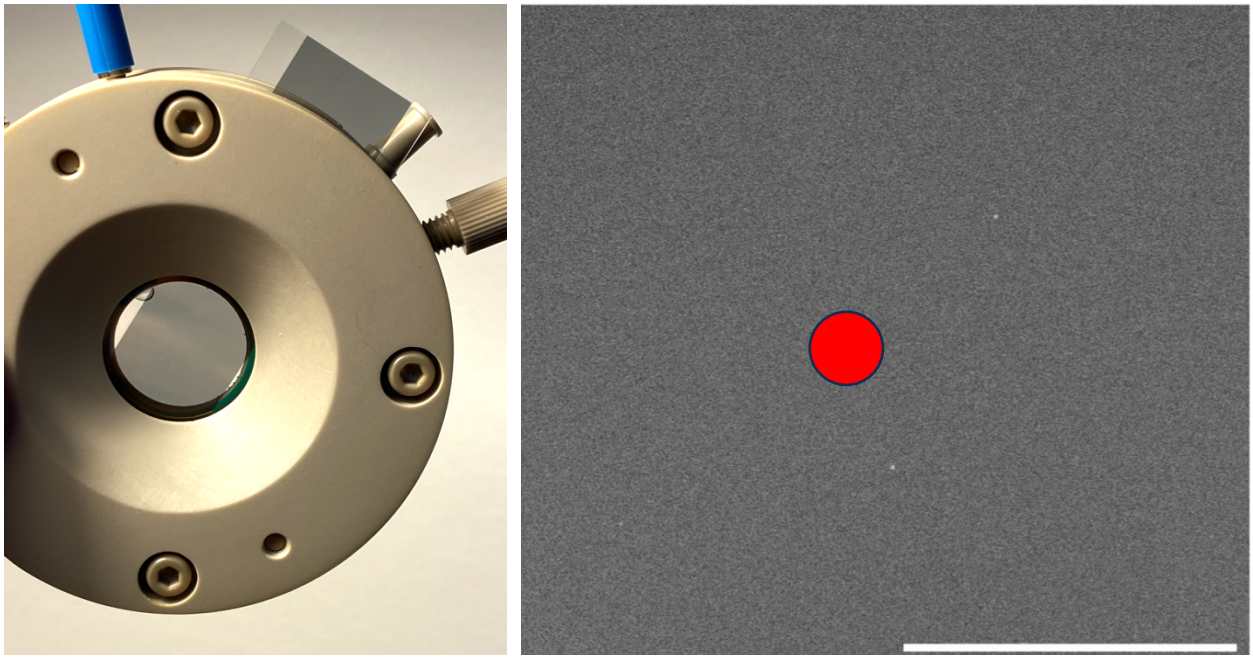

Fig. S7. a) Optical image of a mounted 10 nm thin nickel nanolayer on a standard 3 x 1 in^2 VWR glass microscope slide. **b**) Scanning electron microscope image of a thin nickel nanolayer showing

what appears to be three small pinholes that are observed on rare occasion. The red circle indicates the approximate laser spot size (100 μm). Scale bar=500 μm.

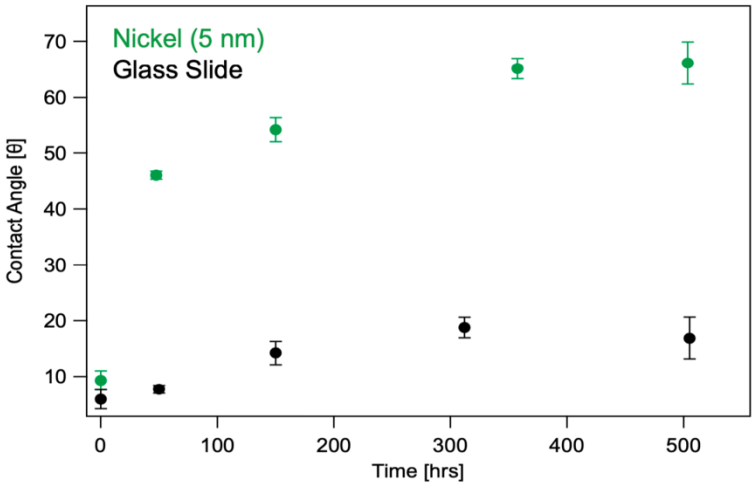

Fig. S8. Water contact angles measured on nickel nanolayers (green) and uncoated glass slides (black) left in ambient laboratory air for the number of hours indicated.

Supplementary Note S1. SHG signals from aqueous electric double layers were first reported by Wang in 1969 (*8*). Heinz and Shen employed electrochemical conditions (*9, 10*), Richmond (*11-16*), Corn (*17, 18*), and Guyot-Sionnest (*19*) pioneered the method in chemistry as electric-field induced second harmonic, and Eisenthal established it for insulators (*20*). The field grew(*21-24*) to include vibrational sum frequency generation (SFG) spectroscopy (*25-31*). Homodyne-detected SFG spectroscopy and SHG microscopy imaging under electrochemical control have now been realized by the Campen and Roke groups for Au electrodes in the electrochemical stability window as well as for the OER (*32-35*). Liu and Shen reported phase-resolved nonlinear optical measurements of optically thin, gate-controlled Si:SiOx:water interfaces (*36*), while the Suntivich group applied phase-sensitive SHG to Pt electrodes to identify potentials of zero charge (*37, 38*).

Supplementary Note S2. We employ a rotating phase shifting unit based on the design by Huang and Lewis (*39*). The interference fringes are fit to the following function, taken from Stolle et al. (*40*):

$$f(\theta) = a + b \cdot (\theta+\delta\theta) + c \cdot (\theta+\delta\theta)^2 + Esig \cdot \cos\{4\pi \cdot [0.00107566/(1.03 \cdot 10^{-6})] \cdot \quad \text{eqn. S1}$$

$$\cdot\{1.4619 \cdot \cos[\text{asin}(\sin((\theta+\delta\theta)/1.4619)] - 1.4501 \cdot \cos[\text{asin}(\sin((\theta+\delta\theta)/1.4501)]\} + \varphi_{fit}\}$$

Here, a is y-axis offset, b and c account for the parabolic profile of the fringes that is due to slight reflection losses at increased angles, θ, of the phase shifting unit (PSU angle, varied by ±40° around 0°), δθ accounts for not being able to mount the PSU to be exactly perpendicular to the entering beams (the true 0°), E_{sig} is the SHG amplitude, the factor 0.00107566 is the value of the fused silica plate thickness from replicate caliper measurements (in meters), $1.03 \cdot 10^{-6}$ is the value of the fundamental wavelength (in meters), 1.4619 and 1.4501 are the refractive indices of fused silica at the second harmonic and fundamental wavelength obtained from a four-parameter Cauchy equation fit to tabulated IR grade fused silica values available from ISP Optics, and φ_{fit} is the fitted SHG phase. Eqn. S1 is fit to each fringe, with a, b, c, δθ, E_{sig} and φ_{fit} as fit parameters. Uncertainties from the IgorPro fitting algorithm are <3% in E_{sig} and <1.5° in φ_{sig}. This technique has also been successfully applied to determine the nonlinear optical phase of gold surfaces in vibrational sum frequency spectroscopy (*40*).

Supplementary Note S3. We obtain the calibration factor, *C*, used in eqns. 1 and 2 as follows: We first measured the SHG intensity from a nickel electrode at pH 13 and 1 M NaCl at OCP (determined to be -0.1 V vs Ag/AgCl using the Autolab OCP-determination program sequence) to be 200 counts per 100 ms, with 0.2 mW input power and the -1 cm defocused lens arrangement described in the main text (see Fig. 1B in the main text). We then replaced the aqueous solution with a piece of z-cut α-quartz aligned as described previously (*4, 41*) and affixed to a glass

microscope slide (no Ni present) using a drop of index matching fluid. The resulting SHG intensity saturated the detector, so we reduced the input energy of the fundamental to 0.1 W. The resulting SHG intensity was measured to be 400,000 counts per 100 ms. Dividing the SHG intensity from the nickel:electrolyte interface measured before by a factor of 4 and taking square roots to obtain the electric field response difference resulted in a factor E_{sample}/E_{quartz}=1/90=0.011.

We then compute the effective second-order nonlinear susceptibility of the α-quartz piece sampled in our optical setup by dividing its bulk second-order nonlinear susceptibility by the wavevector mismatch (2.2 x 10^7 m^{-1} in our setup, using the angles and optical constants indicated in Fig. S5) to obtain a $\chi^{(2)}_{eff,quartz}$=3.0 x 10^{-22} m^2V^{-1}. Multiplying this value by the ratio of the Fresnel coefficients in our window/quartz vs window/electrolyte interface (computed as previously described (*4, 41*) using the angles indicated in Fig. S5, this ratio is 0.58/0.68) yields an estimate for *C* of 3.1 x 10^{-22} m^2V^{-1}.

We note that the model described above treats the ten-nanometer thin nickel:nickel oxide as non-refractory, which experiments confirm that verify the lack of spatial displacement of a visible laser beam passing through the glass slide/nickel electrode as opposed to an uncoated portion of the electrode. We also treat the optical absorbance of the nickel nanolayer at the fundamental and the second harmonic (<20%) to be minor.

Supplementary Note S4. We express the nonlinear optical response from the electrode:electrolyte interface as follows:

$$C \cdot E_{sig,norm} e^{i\varphi_{sig}} = \chi^{(2)} - 5i\chi^{(2)} - \chi_w^{(3)} \Phi(0)_{tot}(1 + 1.5i) \qquad \text{eqn. S1}$$

Here, *C* is the calibration factor estimated as described above, $E_{sig,norm}$ is the measured SHG amplitude normalized to the value obtained at zero applied volt (OCP, the condition at which we calibrate to quartz, as described above), and $\varphi_{sig} = \varphi_{fit,\Phi} - \varphi_{fit,OCP} - 76° \pm 19°$, as described in the

main text. On the right-hand-side of the equation we have $\chi^{(2)}$, the second-order nonlinear susceptibility, the ca. 5-fold larger resonant contribution and its phase of -90° ($e^{-i\pi} = -1$, within the range of the measured 76° ± 19° glass:air to nickel:air phase difference described in the main text), the third-order nonlinear susceptibility of water, $\chi_w^{(3)}$, and the total interfacial potential, $\Phi(0)_{tot}$. We express the left-hand-side of eqn. S1 using the Euler identity and collect the real and imaginary terms to obtain

$$C \cdot E_{sig,norm} cos(\varphi_{sig}) = \chi^{(2)} - \chi_w^{(3)} \Phi(0)_{tot} \quad \text{eqn. S2}$$

$$C \cdot E_{sig,norm} sin(\varphi_{sig}) = -5\chi^{(2)} - 1.5\chi_w^{(3)} \Phi(0)_{tot} \quad \text{eqn. S3}$$

Eqn. 3 is rearranged for $\chi^{(2)}$ to yield

$$\chi^{(2)} = -\frac{C \cdot E_{sig,norm} sin(\varphi_{sig}) + 1.5\chi_w^{(3)} \Phi(0)_{tot}}{5} \quad \text{eqn. S4}$$

Placing this expression for $\chi^{(2)}$ into eqn. S2 then yields the total interfacial potential as

$$\Phi(0)_{tot} = -\frac{C \cdot E_{sig,norm} \{5 \cdot cos(\varphi_{sig}) + sin(\varphi_{sig})\}}{(5+1.5)\chi_{water}^{(3)}} \quad \text{eqn. S5}$$

Supplementary Note S5. The second-order nonlinear susceptibility and (eqn. S4) and especially the total potential (eqn. S5) vary little if the factor 5 in eqn. S1 is changed by ±1 to 4 or 6 (Fig. S9).

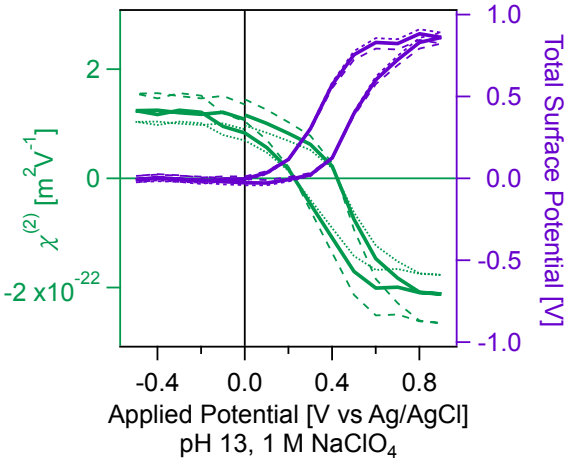

Fig. S9. Second-order nonlinear susceptibility and total surface potential as a function of applied potential computed using a factor of 5 (thick solid lines), 4 (dashed lines), and 6 (dotted lines).

References

1. M. D. Boamah *et al.*, Energy Conversion via Metal Nanolayers. *PNAS* **116**, 16210-16215 (2019).
2. R. R. Rao *et al.*, Spectroelectrochemical Analysis of the Water Oxidation Mechanism on Doped Nickel Oxides. *J. Am. Chem. Sco.* **144**, 7622-7633 (2022).
3. M. D. Boamah, D. Isheim, F. M. Geiger, Dendritic Oxide Growth in Zerovalent Iron Nanofilms Revealed by Atom Probe Tomography. *J. Phys. Chem. C* **122**, 28225-28232 (2018).
4. E. Ma *et al.*, A New Imaginary Term in the 2nd Order Nonlinear Susceptibility from Charged Interfaces. *J. Phys. Chem. Lett.* **12**, 5649-5659 (2021).
5. P. A. Covert, D. K. Hore, Assessing the Gold Standard: The Complex Vibrational Nonlinear Susceptibility of Metals. *J. Phys. Chem. C* **119**, 271-276 (2014).
6. K. Kemnitz *et al.*, The Phase of 2nd-Harmonic Light Generated at an Interface and Its Relation to Absolute Molecular-Orientation. *Chem. Phys. Lett.* **131**, 285-290 (1986).
7. P. E. Ohno, S. A. Saslow, H.-f. Wang, F. M. Geiger, K. B. Eisenthal, Phase-referenced Nonlinear Spectroscopy of the alpha-Quartz/Water Interface. *Nature communications* **7**, 13587 (2016).
8. C. Wang, Second-Harmonic Generation of Light at the Boundary of an Isotropic Medium. *Phys. Rev.* **178**, 1457-1461 (1969).
9. T. F. Heinz, C. K. Chen, D. Ricard, Y. R. Shen, Optical 2nd-Harmonic Generation from a Monolayer of Centrosymmetric Molecules Adsorbed on Silver. *Chemical Physics Letters* **83**, 180-182 (1981).
10. C. K. Chen, T. F. Heinz, D. Ricard, Y. R. Shen, Surface-Enhanced 2nd-Harmonic Generation and Raman-Scattering. *Phys. Rev. B* **27**, 1965-1979 (1983).

11. G. L. Richmond, Surface second harmonic generation from sulfate ions adsorbed on silver electrodes. *Chem. Phys. Lett.* **106**, 26-29 (1984).

12. H. M. Rojhantalab, G. L. Richmond, Interfacial Studies of Silver-Aqueous Electrolytes by Optical 2nd Harmonic and Differential Capacitance. *Journal of the Optical Society of America a-Optics Image Science and Vision* **3**, P52-P53 (1986).

13. G. L. Richmond, Characterization of the Silver Aqueous-Electrolyte Interface by Optical 2nd Harmonic-Generation. *Langmuir* **2**, 132-139 (1986).

14. G. L. Richmond, Adsorption of ions on smooth and roughened silver surfaces: a comparative study by optical second harmonic generation. *Chemical Physics Letters* **113**, 359-363 (1985).

15. G. L. Richmond, H. M. Rojhantalab, J. M. Robinson, V. L. Shannon, Experiments on optical second-harmonic generation as a surface probe of electrodes. *J. Opt. Soc. Am. B-Opt. Phys.* **4**, 228-236 (1987).

16. G. L. Richmond, Insitu Characterization of Solid Liquid Interfaces by Optical 2nd Harmonic-Generation. *Journal of the Electrochemical Society* **134**, C111-C111 (1987).

17. R. M. Corn, M. Romagnoli, M. D. Levenson, M. R. Philpott, The Potential Dependence of Surface Plasmon-Enhanced Second-Harmonic Generation at Thin Film Silver Electrodes. *Chem. Phys. Lett.* **106**, 30-35 (1984).

18. J. M. Lantz, R. M. Corn, Time-Resolved Optical Second Harmonic Generation Measurements of Picosecond Band Flattening Processes at Single Crystal Ti02 Electrodes. *J. Phys. Chem.* **98**, 9387-9390 (1994).

19. P. Guyot-Sionnest, A. Tadjeddine, Study of Ag(111) and Au(111) Electrodes by Optical Second-harmonic Generation. *J. Chem. Phys.* **92**, 734-738 (1990).

20. S. Ong, X. Zhao, K. B. Eisenthal, Polarization of water molecules at a charged interface; second harmonic studies of the silica/water interface. *Chem. Phys. Lett.* **191**, 327-335 (1992).

21. G. L. Richmond, J. M. Robinson, V. L. Shannon, 2nd Harmonic-Generation Studies of Interfacial Structure and Dynamics. *Progress in Surface Science* **28**, 1-70 (1988).

22. R. M. Corn, D. A. Higgins, Optical Second Harmonic Generation as a Probe of Surface Chemistry. *Chem. Rev.* **94**, 107 (1994).

23. K. B. Eisenthal, Liquid interfaces probed by second-harmonic and sum-frequency spectroscopy. *Chem. Rev.* **96**, 1343-1360 (1996).

24. K. B. Eisenthal, Second Harmonic Spectroscopy of Aqueous Nano- and Microparticle Interfaces *Chem. Rev.* **106**, 1462-1477 (2006).

25. S. Baldelli, N. Markovic, P. Ross, Y. R. Shen, G. Somorjai, Sum frequency generation of CO on (111) and polycrystalline platinum electrode surfaces: Evidence for SFG invisible surface CO. *J. Phys. Chem. B* **103**, 8920-8925 (1999).

26. S. Baldelli, G. Mailhot, P. Ross, Y. R. Shen, G. A. Somarjai, Potential dependent orientation of acetonitrile on platinum (111) electrode surface studied by sum frequency generation. *Journal of Physical Chemistry B* **105**, 654-662 (2001).

27. S. Baldelli, Probing Electric Fields at the Ionic Liquid-Electrode Interface Using Sum Frequency Generation Spectroscopy and Electrochemistry. *J. Phys. Chem. B* **109**, 13049-13051 (2005).

28. S. K. Shaw, A. Lagutchev, D. D. Dlott, A. A. Gewirth, Electrochemically Driven Reorientation of Three Ionic States of p-Aminobenzoic Acid on Ag(111). *The Journal of Physical Chemistry C* **113**, 2417-2424 (2009).

29. S. K. Shaw, A. Lagutchev, D. D. Dlott, A. A. Gewirth, Sum-Frequency Spectroscopy of Molecular Adsorbates on Low-index Ag Surfaces: Effects of Azimuthal Rotation. *Analytical Chemistry* **81**, 1154-1161 (2009).

30. N. Garcia Rey, D. D. Dlott, Structural Transition in an Ionic Liquid Controls CO2 Electrochemical Reduction. *J. Phys. Chem. C* **119**, 20892-20899 (2015).

31. N. Garcia Rey, D. D. Dlott, Studies of electrochemical interfaces by broadband sum frequency generation. *J. Electroanal. Chem.* **800**, 114-125 (2017).

32. Y. Tong, K. Cai, M. Wolf, R. K. Campen, Probing the electrooxidation of weakly adsorbed formic acid on Pt(1 0 0). *Catalysis Today* **260**, 66-71 (2016).

33. Y. Tong, F. Lapointe, M. Thaemer, M. Wolf, R. K. Campen, Experimentally Probing Hydrophobic Water at the Gold Electrode / Aqueous Interface. *Angew. Chemie Int. Ed.* **56**, 4211-4214 (2017).

34. I. Nahalka, G. Zwaschka, R. K. Campen, A. Marchioro, S. Roke, Mapping Electrochemical Heterogeneity at Gold Surfaces: A Second Harmonic Imaging Study. *J. Phys. Chem. C* **124**, 20021-20034 (2020).

35. G. Zwaschka *et al.*, Imaging the Heterogeneity of the Oxygen Evolution Reaction on Gold Electrodes Operando: Activity is Highly Local. *ACS Catalysis* **10**, 6084-6093 (2020).

36. H. Wang *et al.*, Gate-Controlled Sum-Frequency Vibrational Spectroscopy for Probing Charged Oxide/Water Interfaces. *J. Phys. Chem. Lett.* **10**, 5943-5948 (2019).

37. P. Xu, A. Huang, J. Suntivich, Phase-Sensitive Second-Harmonic Generation of Electrochemical Interfaces. *J. Phys. Chem. Lett.* **11**, 8216-8221 (2020).

38. P. Xu, A. D. von Rueden, R. Schimmenti, M. Mavrikakis, J. Suntivich, Optical method for quantifying the potential of zero charge at the platinum-water electrochemical interface. *Nature Materials* **22**, 503-510 (2023).

39. J. Y. Huang, A. Lewis, Determination of the absolute orientation of the retinylidene chromophore in purple membrane by a second-harmonic interference technique. *Biophys. J.* **55**, 835-842 (1989).

40. R. Stolle, G. Marowsky, E. Schwarzberg, G. Berkovic, Phase measurements in nonlinear optics. *Appl. Phys. B* **63**, 491-498 (1996).

41. E. Ma, F. M. Geiger, Divalent Ion Specific Outcomes on Stern Layer Structure and Total Surface Potential at the Silica:Water Interface. *Journal of Physical Chemistry A* **125**, 10079-10088 (2021).